Combustion-Thermoelectric Tube

C.-W. Park

M. Kaviany[1]
e-mail: kaviany@umich.edu

Department of Mechanical Engineering,
The University of Michigan,
Ann Arbor, MI 48109-2125

In direct combustion-thermoelectric energy conversion, direct fuel injection and reciprocation of the air flowing in a solid matrix are combined with the solid-gas interfacial heat transfer and the solid conduction to allow for obtaining superadiabatic temperatures at the hot junctions. While the solid conductivity is necessary, the relatively large thermal conductivity of the available high-temperature thermoelectric materials (e.g., Si–Ge alloys) results in a large conduction loss from the hot junctions and deteriorates the performance. Here, a combustion-thermoelectric tube is introduced and analyzed. Radially averaged temperatures are used for the fluid and solid phases. A combination of external cooling of the cold junctions, and direct injection of the fuel, has been used to increase the energy conversion efficiency for low thermal conductivity, high-melting temperature thermoelectric materials. The parametric study (geometry, flow, stoichiometry, materials) shows that with the current high figure of merit, high temperature $Si_{0.7}Ge_{0.3}$ properties, a conversion efficiency of about 11 percent is achievable. With lower thermal conductivities for these high-temperature materials, efficiencies about 25 percent appear possible. This places this energy conversion in line with the other high efficiency, direct, electric power generation methods. [S0022-1481(00)01304-9]

Keywords: Combustion, Energy Conversion, Heat Transfer, Optimization, Thermoelectric

Introduction

Local, superadiabatic temperatures are obtained in premixed combustion in porous media by gas preheating (i.e., heat recirculation) through the solid matrix. Hanamura et al. [1] have designed a reciprocating premixed fluid flow-porous medium system to create such super-adiabatic temperatures. The release of the heat of combustion in the gas phase is followed by the solid-gas interfacial heat transfer and solid-phase conduction and radiation. The interfacial heat transfer to the upstream cold gaseous stream completes the heat recirculation and the formation of local, superadiabatic temperatures in the flame region ([2–5]). The important roles of the interfacial surface area per unit volume, the Nusselt number, and the reciprocation of the flow, are evident in this heat recirculation. As compared to the unidirectional flow arrangement used for achieving a superadiabatic flame temperature by solid conduction (and surface radiation), the reciprocation of the flow allows for heat recirculation using the storage/release of the thermal energy in the solid. The lack of solid conductivity and surface radiation would assist the process.

Echigo et al. [6] have also suggested that such a system can be harvested for thermoelectric energy conversion by placing the hot junction in the flame region and the cold junction in the entrance region (one on each side). A relatively short combustion region separates the two thermoelectric regions. Critical to the high efficiency of this combustion-thermoelectric system is the solid conductivity in the thermoelectric region. The currently available high-temperature thermoelectric materials ([7]), have relatively high figure of merits (e.g., Si–Ge alloys), while also having relatively high thermal conductivities which prevent high energy-conversion efficiencies. These high-temperature ceramics are fabricated from powders and the effective conductivity of the sintered powder mixture is much smaller than the bulk thermal conductivity of each of the components and depends on their grain sizes. It has been shown by Chen [8] that the effective conductivity can be reduced by using very fine grains. The search for low conductivity thermoelectric materials continues.

The use of direct fuel injection, as compared to premixing, allows for a better control of the flame location and further increases the maximum gas and solid temperatures avoiding any premature ignition ([9]).

Here in order to identify the potential and limitation of this energy conversion system, a combustion-thermoelectric tube is introduced and analyzed. The tube is shown in Fig. 1(*a*). The reciprocating oxidant (here air is used) flow is represented by a radially averaged fluid velocity $\langle u \rangle_g$ which alters in direction at the end of each half cycle. The tube consists of two thermoelectric regions (designated by TE) and one combustion region (designated by *C*). The combustion region is much shorter than each of the thermoelectric regions. The tube inside and outside diameters are uniform throughout. In the thermoelectric region, the tube wall is made of a layer of *p*-type and a layer of *n*-type semiconductor materials with a very thin (neglected thickness) dielectric layer (such as a silicon oxide) separating these two layers. The thermoelectric and combustion regions are connected with an assumed negligible thermal contact resistance.

The fuel (gaseous methane) is injected laterally in a short combustion region. Due to the small diameter tube (order of one millimeter), the fuel is expected to mix over a short distance. Using radial diffusion only, the distance needed for the penetration of the fluid supplied at the periphery is $0.01\langle u \rangle_{g,o} D_1^2 / D_m$. For the range of $\langle u \rangle_{g,o}$, D_1, and D_m (and T_g) considered here, this distance is less than the tube diameter D_1. Also, due to the high temperature of the combustion region and the availability of the oxidant (i.e., low stoichiometry, fuel-limited combustion), the fuel is completely burned.

There are geometrical parameters (diameters and lengths), flow parameters (velocity and cycle period), heat transfer parameters (Nusselt number, surface emissivity), fuel parameters (stoichiometric ratio), thermoelectric material properties (Seebeck coefficient, thermal conductivity, electrical resistivity), and power-circuit parameter (external resistance). Through parametric variations, the role of these parameters on the thermoelectric energy conversion is studied using the properties of one of the current high-temperature thermoelectric materials, i.e., $Si_{0.7}Ge_{0.3}$ alloys. Then further increase in the efficiency is demonstrated with a reduction in the thermal conductivity.

[1]To whom correspondence should be addressed.

Contributed by the Heat Transfer Division for publication in the JOURNAL OF HEAT TRANSFER. Manuscript received by the Heat Transfer Division, Feb. 20, 1999; revision received, June 5, 2000. Associate Technical Editor: J. P. Gore.

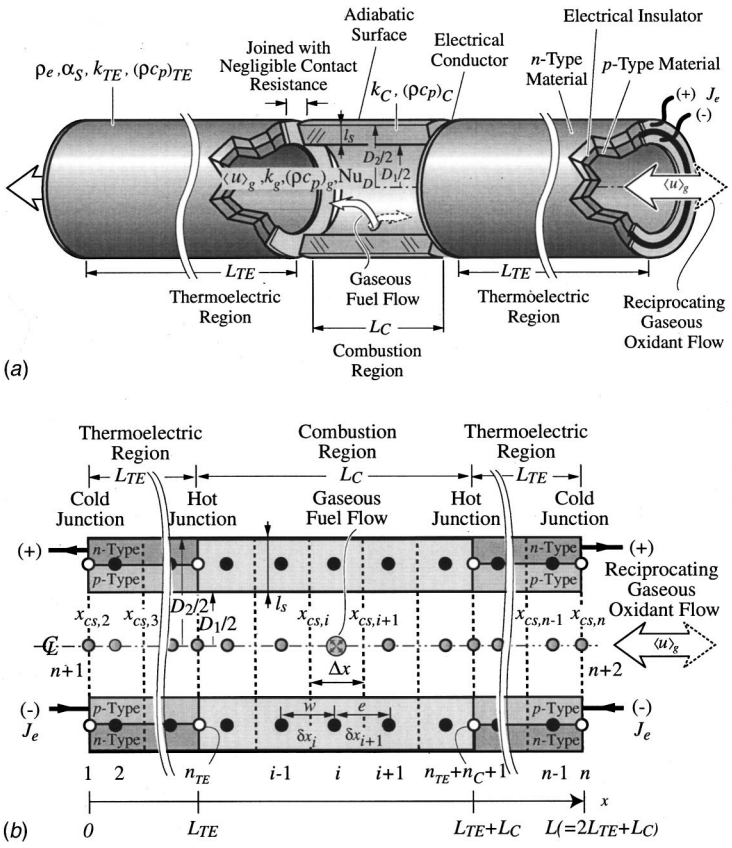

Fig. 1 (*a*) A schematic of the combustion-thermoelectric tube; (*b*) thermal nodal model of the combustion-thermoelectric tube.

Analysis

Radially averaged temperatures are used for the gas and solid phases. The various regions are axially divided into small, finite volumes. These volumes are shown in Fig. 1(*b*). The surface nodes are shown with open circles and they are at the cold and hot junctions, i.e., at $i=1$, n_{TE}, $n_{\mathrm{TE}}+n_C+1$, and n. Constant thermophysical properties and a unity Lewis number (Le=1), are assumed.

Using the radially averaged velocity $\langle u\rangle_g$, the mass conservation equation for the gas phase is

$$A_g\Delta x\frac{d\rho_{g,i}}{dt}=(\rho A\langle u\rangle)_{g,w,i}-(\rho A\langle u\rangle)_{g,e,i}. \tag{1}$$

The density is given by the ideal gas law, $\rho_g=pM_g/\bar{R}T_g$, and a constant, atmospheric pressure is assumed.

The finite-volume species mass conservation equation for the product-species P in i gas-phase node is

$$A_g\Delta x\frac{d}{dt}\frac{\rho_{\mathrm{P},i}}{\rho_g}=A_g[(\rho_{\mathrm{P}}\langle u\rangle_g)_{w,i}-(\rho_{\mathrm{P}}\langle u\rangle_g)_{e,i}]+D_mA_g\left(\frac{\rho_{\mathrm{P},i-1}-\rho_{\mathrm{P},i}}{\delta x_i}-\frac{\rho_{\mathrm{P},i}-\rho_{\mathrm{P},i+1}}{\delta x_{i+1}}\right)+\dot{n}_{r,\mathrm{P},i}A_g\Delta x, \tag{2}$$

where i is the axial node index.

For the product species generation terms $\dot{n}_{r,\mathrm{P},i}$, a first-order, Arrhenius relation ([10]) is used, i.e.,

$$\dot{n}_{r,\mathrm{P},i}=a_r(\rho_g-\rho_{\mathrm{P},i})e^{-\Delta E_a/\bar{R}T_{g,i}}, \tag{3}$$

where $\rho_{g,i}=\rho_{\mathrm{R},i}+\rho_{\mathrm{P},i}$, $\rho_{\mathrm{R},i}=\rho_{\mathrm{F},i}+\rho_{\mathrm{O},i}$ and $(\rho_{g,i}-\rho_{\mathrm{P},i})$ is the local reactant density in the gas phase. Since the amount of the injected fuel (2.36 percent of the oxidant mass flow rate for the baseline conditions) is small, it is assumed that the injected fuel is well mixed and the change in ρ_g due to the fuel injection is negligible and a premixed reaction begins after the injection.

The two medium model is used here to allow for the thermal nonequilibrium caused by the gaseous combustion. The radially averaged temperatures $\langle T\rangle_r^g=T_g$ and $\langle T\rangle_r^s=T_s$ are used, where $\langle\,\rangle_r^g$ and $\langle\,\rangle_r^s$ indicate radially, phase averaged quantities ([11]).

The finite-volume energy conservation equation for the i gas-phase node [shown in Fig. 1(*b*)] is

$$A_g\Delta x\frac{d}{dt}(\rho c_pT)_{g,i}=Q_{g,u,i}+Q_{g,k,i}+Q_{g,ku,i}+\dot{S}_{r,c,i}, \tag{4}$$

where

$$Q_{g,u,i}=(\rho c_p\langle u\rangle AT)_{g,w,i}-(\rho c_p\langle u\rangle AT)_{g,e,i} \tag{5}$$

$$Q_{g,k,i}=k_gA_g\left(\frac{T_{g,i-1}-T_{g,i}}{\delta x_i}-\frac{T_{g,i}-T_{g,i+1}}{\delta x_{i+1}}\right) \tag{6}$$

$$Q_{g,ku,i}=\mathrm{Nu}_D\frac{k_g}{D_1}A_{sg}(T_{s,i}-T_{g,i}) \tag{7}$$

$$\dot{S}_{r,c,i}=-\Delta h_{r,F}\frac{\nu_{\mathrm{F}}M_{\mathrm{F}}}{\nu_{\mathrm{R}}M_{\mathrm{R}}}\dot{n}_{r,\mathrm{P},i}A_g\Delta x. \tag{8}$$

The hydrodynamic dispersion is neglected, because of the small Péclet number and the dominance of the surface convection over gaseous conduction and dispersion. The energy equation for the i solid-phase node [shown in Fig. 1(*b*)] is

$$(\rho c_p)_{s,i} A_s \Delta x \frac{dT_{s,i}}{dt} = Q_{s,k,i} - Q_{s,ku,i} - Q_{s,r,i} + (\dot{S}_{e,J})_i + (\dot{S}_{e,P})_i , \tag{9}$$

where

$$Q_{s,k,i} = k_s A_s \left(\frac{T_{s,i-1} - T_{s,i}}{\delta x_i} - \frac{T_{s,i} - T_{s,i+1}}{\delta x_{i+1}} \right) \tag{10}$$

$$Q_{s,ku,i} = \mathrm{Nu}_D \frac{k_g}{D_1} A_{sg} (T_{s,i} - T_{g,i}) \tag{11}$$

$$Q_{s,r,i} = \frac{E_{b,i} - (q_{r,o})_i}{\left(\frac{1-\epsilon_r}{A_r \epsilon_r} \right)_i} \tag{12}$$

$$(\dot{S}_{e,J})_i = \left[\left(\frac{\rho_e \Delta x}{A} \right)_{p,i} + \left(\frac{\rho_e \Delta x}{A} \right)_{n,i} \right] J_e^2 \quad \text{for TE region} \tag{13}$$

$$(\dot{S}_{e,P})_i = \mp \alpha_S T_{s,i} J_e \quad \text{at hot/cold junctions of TE region,} \tag{14}$$

where the Nusselt number, Nu_D, is taken to be for laminar, fully developed fields, occuring $\mathrm{Re}_D < 2300$, $\mathrm{Nu}_D = 3.66$. The Peltier heat absorption/release $(\dot{S}_{e,P})_i$ occurs at the hot/cold junctions and is used in the surface nodes.

Using simple mean beam length analysis ([12]), it can be shown that for small (order of one millimeter diameter) tubes, the gas radiation is less than one half percent of the surface radiation. The surface radiation heat flow rate $Q_{s,r,i}$ is written as

$$Q_{s,r,i} = \frac{E_{b,i} - (q_{r,o})_i}{\left(\frac{1-\epsilon_r}{A_r \epsilon_r} \right)_i} = \sum_{j=1}^{n+2} \frac{(q_{r,o})_i - (q_{r,o})_j}{\frac{1}{A_{r,i} F_{i-j}}}, \tag{15}$$

where $E_{b,i} = \sigma_{\mathrm{SB}} T_{s,i}^4$ is the total hemispherical blackbody emissive power. The inlet $(i = n+1)$ and outlet region $(i = n+2)$ of the tube as shown in Fig. 1(*b*), are treated as imaginary blackbody surfaces. The view factor F_{i-j} is obtained by the kernel approximation ([2,12]) and is

$$F_{i-j} = \frac{D_1}{4\Delta x} [e^{2(x_{cs,i} + \Delta x)/D_1} - e^{2x_{cs,i}/D_1}] \times [e^{-2x_{cs,j}/D_1} - e^{-2(x_{cs,j} + \Delta x)/D_1}]$$
$$i, j = 1, \ldots, n \quad \text{ring to another ring} \tag{16}$$

$$F_{i-j} = \frac{D_1}{4\Delta x} [e^{-2x_{cs,i}/D_1} - e^{-2(x_{cs,i} + \Delta x)/D_1}]$$
$$i = 1, \ldots, n, \; j = n+1, n+2 \quad \text{ring to end disk.} \tag{17}$$

Figure 2(*a*) shows a bundle of the combustion-thermoelectric tubes with its electrical connections. Figure 2(*b*) also shows the electrical circuit for such a bundle. The voltage $\Delta\varphi$ for an N_t-tube bundle shown in Fig. 2(*b*), is

$$\Delta\varphi = J_e R_{e,o} = 2N_t [\alpha_S \Delta T_s - J_e (R_{e,p} + R_{e,n})], \tag{18}$$

where $\Delta T_s = T_{s,h} - T_{s,c}$, $T_{s,h} = (T_{s,n_{\mathrm{TE}}} + T_{s,n_{\mathrm{TE}}+n_C+1})/2$, $T_{s,c} = (T_{s,1} + T_{s,n})/2$, $\alpha_S = \alpha_{S,p} - \alpha_{S,n}$, $R_{e,p} = (\rho_e L/A)_p$ and $R_{e,n} = (\rho_e L/A)_n$.

For the case of $A_p = A_n = A_s/2$, $\rho_{e,p} = \rho_{e,n} = \rho_e$ and $L_p = L_n = L_{\mathrm{TE}}$, the internal electrical resistance of the left side of a thermoelectric tube, shaded in Fig. 2(*b*), is

$$R_e = R_{e,p} + R_{e,n} = \left(\frac{\rho_e L}{A} \right)_p + \left(\frac{\rho_e L}{A} \right)_n = 4 \frac{\rho_e L_{\mathrm{TE}}}{A_s}, \tag{19}$$

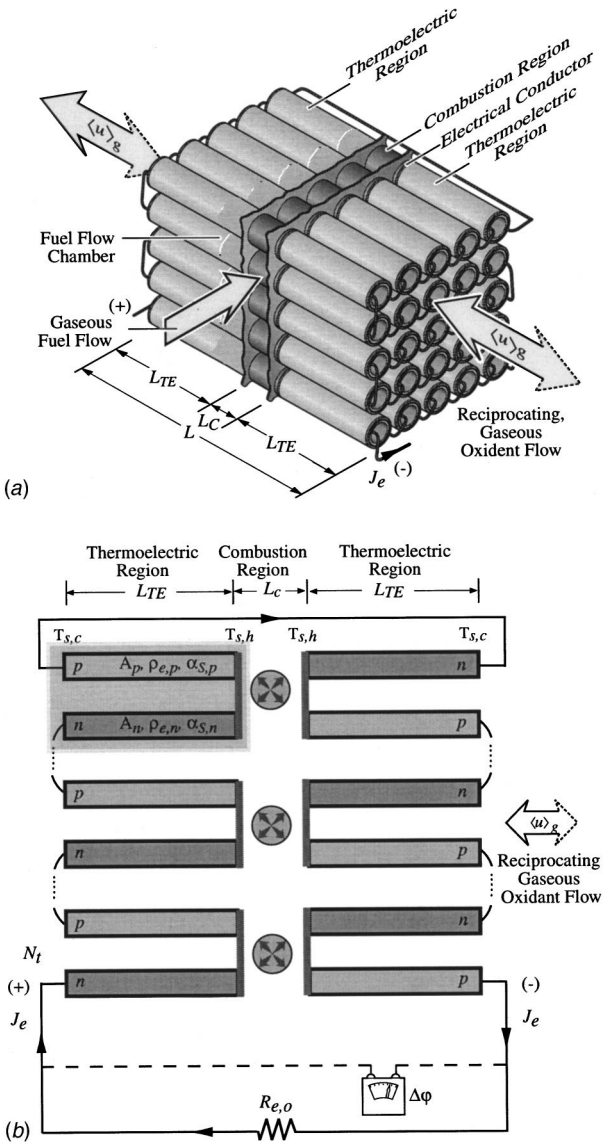

Fig. 2 (*a*) Tube-bundle module of the combustion-thermoelectric energy converter; (*b*) electrical circuit for the combustion-thermoelectric energy converter

where A_p and A_n are the cross-sectional areas of the *p*-type and *n*-type thermoelectric materials, and A_s is the total solid cross-sectional area.

Using the voltage relation, Eq. (18), the current is

$$J_e = \frac{2N_t \alpha_S \Delta T_s}{2N_t R_e + R_{e,o}} = \frac{\alpha_S \Delta T_e}{R_e (1 + R_{e,o}^*)} = \frac{\alpha_S \Delta T_s}{4\rho_e L_{\mathrm{TE}} (1 + R_{e,o}^*)} A_s , \tag{20}$$

where $R_{e,o}^*$ is the ratio of the external resistances to the internal resistance, i.e., $R_{e,o}/(2N_t R_e)$.

The electric power generated is

$$J_e^2 R_{e,o} = 2N_t (J_e \alpha_S \Delta T_s - J_e^2 R_e)$$
$$= N_t \frac{\alpha_S^2 \Delta T_s^2 R_{e,o}^*}{2\rho_e L_{\mathrm{TE}} (1 + R_{e,o}^*)^2} A_s . \tag{21}$$

The gas-phase energy and species-*P* conservation equations for the inlet and outlet fluid nodes, for the gas flowing from left to right, are

$$-k_g A_g \frac{T_{g,1}-T_{g,2}}{\delta x_2}+(\rho c_p A)_g \langle u\rangle_g (T_o-T_{g,1})=0 \quad \text{at } i=1 \tag{22}$$

$$T_{g,n}=T_{g,n-1} \quad \text{at } i=n \tag{23}$$

$$-D_m A_g \frac{\rho_{P,1}-\rho_{P,2}}{\delta x_2}-A_g \langle u\rangle_g \rho_{P,1}=0 \quad \text{at } i=1 \tag{24}$$

$$\rho_{P,n}=\rho_{P,n-1} \quad \text{at } i=n. \tag{25}$$

Similar equations are written for the gas flow from right to left.

The energy equations for the left-side cold junction is

$$-k_{TE}A_s \frac{T_{s,1}-T_{s,2}}{\delta x_2}-\epsilon_r \sigma_{SB} A_s (T_{s,1}^4-T_o^4)+J_e \alpha_s T_{s,1}$$

$$-\mathrm{Nu}_e \frac{k_g}{D_2} A_s (T_{s,1}-T_o)=0, \tag{26}$$

where Nu_e is the external Nusselt number for the external air cooling at cold junctions. A similar equation is written for the right-side cold junction.

Table 1 Physical, chemical, and geometrical properties and the baseline magnitude of parameters.

Parameter	Magnitude
fuel (methane):	
$\rho_{F,o}$	0.02746 kg fuel/m^3
$(\rho_{F,o})_{st}$	0.06424 kg fuel/m^3
Φ	0.414
$\Delta h_{r,F}$	−55.53 MJ/kg fuel
ΔE_a	131 MJ/kmole
a_r	2.8×10^8 1/s
T_{ad}/T_o	4.0
oxidant (air):	
$\rho_{g,o}$	1.164 kg/m^3
$c_{p,g}$	1099 J/kg K
k_g	0.0573 W/m K
μ_g	369.8×10^{-7} N s/m^2
$\langle u\rangle_{g,o}$	0.75 m/s
$T_{g,o}, T_o$	298 K, 298 K
$\mathrm{Nu}_D, \mathrm{Nu}_e$	3.66, 1.5
Re_D	54.5
τ_c	10 s
Le	1
tube bundle module:	
length, $2L_{TE}+L_C$	127.5 mm
cross-sectional area, $a\times a$	30×30 mm^2
number of tubes, N_t	$a^2/D_2^2=144$
electrical resistance ratio	$R_{e,o}^*=1$
power generated	24.0 W, 26.7 kW/m^2
voltage	93.7 V
current	256.3 mA
thermoelectric region $Si_{0.7}Ge_{0.3}$:	
Z_eT_o	0.59
$\alpha_{S,p}, \alpha_{S,n}, \alpha_S(=\alpha_{S,p}-\alpha_{S,n})$	195.3, −207.3, 402.6 μV/K
ρ_e	19.1 μOhm m
ρ_s	2990 kg/m^3
$c_{p,s}$	816.7 J/kg K
C_{TE}	1908.8
k_{TE} (k_{TE}^*)	4.3 W/m K (75)
D_1	1.3 mm
l_s (D_2)	0.6 mm (2.5 mm)
L_{TE}	60 mm
ϵ_r	1.0
T_{sl}	2000 K
combustion region SiC (CVD fabrication):	
ρ_s	3160 kg/m^3
$c_{p,s}$	1310 J/kg K
C_C	3236.0
k_C (k_C^*)	30 W/m K (523.6)
L_C	7.5 mm
ϵ_r	1.0
T_{sl}	3100 K

The thermoelectric conversion efficiency is the ratio of the electric power generated to the combustion heating rate, i.e.,

$$\eta=\frac{J_e^2 R_{e,o}}{-N_t \Delta h_{r,F} \frac{\nu_F M_F}{\nu_R M_R} \rho_g \langle u\rangle_{g,o} A_g}=\frac{\alpha_S^2 \Delta T_s^2 R_{e,o}^*}{\frac{2\rho_e L_{TE}(1+R_{e,o}^*)^2}{A_s}-\Delta h_{r,F}\rho_{F,o}\langle u\rangle_{g,o}A_g}. \tag{27}$$

The power consumed for the reciprocating flow and in other components (e.g., valves), are neglected.

Considering the existence of many parameters, they are made dimensionless reducing their number. The nondimensional parameters are

$$Z_eT_o=\frac{\alpha_S^2}{\rho_e k_{TE}}T_o, \quad R_{e,o}^*=\frac{R_{e,o}}{2N_tR_e}, \quad \mathrm{Re}_D=\frac{\rho_g\langle u\rangle_{g,o}D_1}{\mu_g},$$

$$C=\frac{\rho c_p}{(\rho c_p)_g}, \quad k^*=\frac{k}{k_g}, \quad \Phi=\frac{\rho_{F,o}}{(\rho_{F,o})_{st}}\frac{(1-\rho_{F,o}/\rho_g)_{st}}{(1-\rho_{F,o}/\rho_g)}.$$

The magnitude for the baseline parameters (i.e., conditions) are listed in Table 1 (properties from ([13])). From these magnitudes, the magnitudes of the nondimensional parameters are $Z_eT_o=0.59$, $R_{e,o}^*=1$, $\mathrm{Re}_D=54.5$, $C_{TE}=1908.8$, $C_C=3236.0$, $k_{TE}^*=75$, $k_C^*=523.6$, and $\Phi=0.414$.

The species and energy conservation equations [Eqs. (2), (4) and (9)] are discretized with a central-difference scheme with respect to space, and an implicit-difference scheme with respect to time and are solved simultaneously using iterations ([14]). The grid-net size dependence is tested and for an 85 node (uniform gridnet), an asymptotic solution is obtained. For a typical case, the computation time is about 90 min with HP B160L. The convergence at each time step is obtained by evaluating the residues in the species and energy conservation equations and requiring the maximum residues be below 0.00001. The quasi-steady solution is obtained when the error in the overall energy balance is below 1∼2 percent.

Results and Discussion

Typical results for the distributions of the solid- and gas-phase temperatures, the mass fraction of the combustion products, and the reaction rate at the end of a half cycle, with gas flowing from left to right, are shown in Fig. 3. The results show that for $Si_{0.7}Ge_{0.3}$ alloy with an assumed melting temperature of $T_{sl}=2000$ K, the conversion efficiency is 11.3 percent and the power converted is 24.0 W, under the baseline conditions listed in Table 1.

As was indicated in the introduction, the pure lateral diffusion transport of the fuel is expected to occur in a very short distance. The lateral momentum of the fuel can further assist in the mixing. As shown in Fig. 3, due to the high oxidant temperature, the flame temperature reaches a local, superadiabatic temperature right at the fuel-injection site in the combustion region. The adiabatic flame temperature T_{ad} is also shown in Fig. 3.

The conduction heat flow towards, and the Peltier heat release at the cold junctions, are removed by the intensive external cooling [the product of the total solid cross-sectional area A_s and the external Nusselt number Nu_e is large in Eq. (26)]. A Nusselt number $\mathrm{Nu}_e=150$ (based on the outside diameter) and a surface area A_s are used as a baseline values. When an extended surface (fins) is used with an area of $A=100A_s$, the Nusselt number Nu_e is then reduced to 1.5 which can readily be achieved using low speed air flow over fins.

For $R_{e,o}^*=1$ [obtained as the optimum value for a maximum power from Eq. (21)], the current is independent of the number of tubes, as evident from Eq. (20). The number of tubes in a tube-bundle module, which is an elemental unit circuit, is chosen to meet electrical specifications such as a desired current-voltage. A

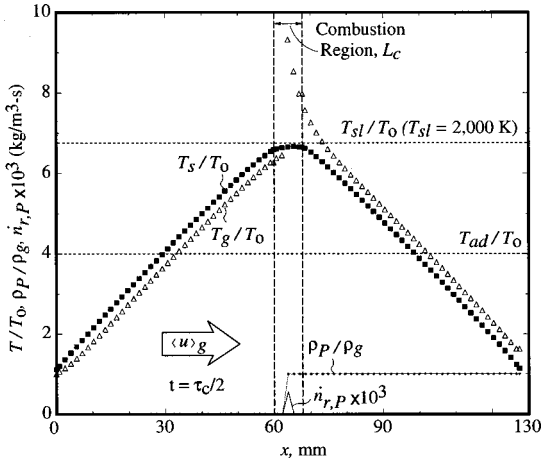

Fig. 3 Typical axial distributions of normalized gas and solid temperatures, reaction rate, and product species mass fraction. $Z_eT_o=0.59$, $R^*_{e,o}=1$, $\tau_c=10$ s, $\langle u\rangle_{g,o}=0.75$ m/s, $D_1=1.3$ mm, $l_s=0.6$ mm, $L_{TE}=60$ mm, $L_C=7.5$ mm, $C_{TE}=1908.8$, $C_C=3236.0$, $k^*_{TE}=75$, $k^*_C=523.6$, $\Phi=0.414$.

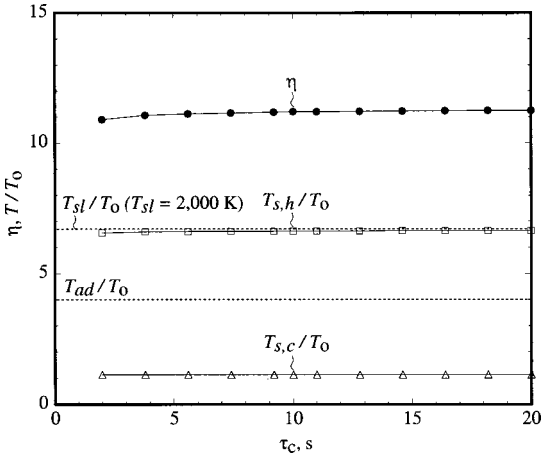

Fig. 4 Effect of the cycle period τ_c on the conversion efficiency and the junction temperatures. $Z_eT_o=0.59$, $R^*_{e,o}=1$, $\langle u\rangle_{g,o}=0.75$ m/s, $D_1=1.3$ mm, $l_s=0.6$ mm, $L_{TE}=60$ mm, $L_C=7.5$ mm, $C_{TE}=1908.8$, $C_C=3236.0$, $k^*_{TE}=75$, $k^*_C=523.6$, $\Phi=0.414$.

tube-bundle module of 144 tubes gives a current of $J_e=256.3$ mA and a voltage of $\Delta\varphi=93.7$ V. For nine such modules connected in parallel, the power is $J_e\Delta\varphi=216.1$ W and the current is $J_e=2.31$ A. Each tube-bundle module has a length $2L_{TE}+L_C=127.5$ mm and a cross-sectional area $a\times a=30\,(\text{mm})\times 30\,(\text{mm})$, in a close-pack, square-array arrangement of the tubes, giving the power density of 26.7 kW/m^2. These results are not far to the design results of the $2L_{TE}+L_C$ of 50 $\sim$100 mm and power density of 5$\sim$10 kW/m^2 suggested by Echigo et al. [6].

Effect of Various Parameters. A parametric study is performed using the fluid flow, thermoelectric-region, and combustion-region parameters. The baseline conditions are listed in Table 1.

Figure 4 shows that the conversion efficiency η, defined by Eq. (27), and the hot and cold junction temperatures of the thermoelectric region, do not change noticeably with the cycle period τ_c. This is because the flame location is fixed at the fuel injection site and due to the intensive external cooling of the cold junction, the transient variations are diminished, as compared to the case of the premixed combustion. For mechanical maintenance purposes, less mechanical movement of the parts (e.g., valves) is desirable. Here, a longer period of $\tau_c=10$ s is used as the baseline condition.

Figure 5 shows that for the gas velocities $\langle u\rangle_{g,o}>0.75$ m/s, the efficiency no longer increases and the hot junction temperature reaches the melting temperature T_{sl}. The pressure drop under the baseline conditions is about 178 Pa, and therefore, is considered rather small.

The combustion region provides as an extended surface to the hot junctions (joined with an assumed negligible contact resistance to the combustion region) for the transfer of the heat released by combustion. Figure 6 shows the effect of the combustion region length L_C (with the fuel injection located at the center of the region), on the conversion efficiency. The effect is not significant, because of the relatively high thermal conductivity for the combustion region, which results in a uniform temperature. For complete combustion, only a short combustion region is needed, i.e., $L_C=7.5$ mm. The efficiency is not very sensitive to the thermal conductivity and the heat capacity of the combustion region. Here, SiC has been used, due to its high melting temperature. The thermal conductivity of SiC varies depending on the fabrication technique (e.g., CVD, sintered powder, etc.). Here a value close to the CVD fabrication is used ([11]).

Figure 7 shows the effect of the stoichiometric ratio Φ on the conversion efficiency η, for several tube wall thicknesses. As the stoichiometric ratio increases, the efficiency and the hot junction temperatures $T_{s,h}$ increase. Above a tube wall thickness $l_s=0.6$ mm used as the baseline value, the efficiency reaches an asymptotic value, with $T_{s,h}$ kept below $T_{sl}=2000$ K. The maximum flame temperature for the tube wall thickness $l_s=0.8$ mm and 0.9 mm, are also shown in Fig. 7. Since the maximum flame temperature depends on the gas preheating temperature (determined by the maximum temperature of the thermoelectric region, i.e., the hot junction temperature $T_{s,h}$), it is much higher than the adiabatic flame temperature. Note that due to the preheating, the flammability limit is reduced significantly. The smallest equivalence ratio for a stable flame in ceramic foams is 0.026 reported by Hoffmann et al. [5].

The oxidant preheating temperature is determined by the length of the thermoelectric region L_{TE}. The flame has a superadiabatic temperature and as compared to the premixed combustion, the flame position is determined by the fuel injection location, instead of the ignition temperature. In addition, with the fuel injection the maximum flame temperature is only limited by the allowable maximum temperature of the combustion region, i.e., its the melt-

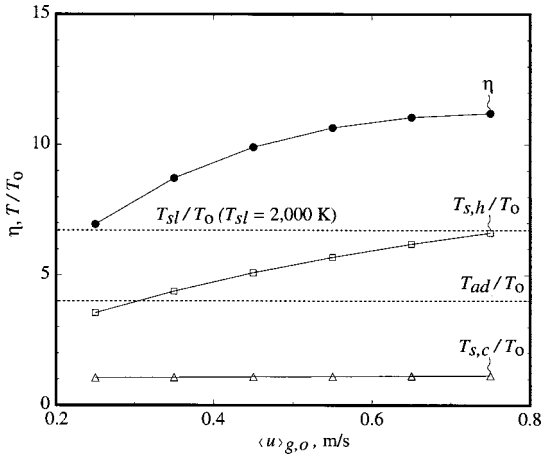

Fig. 5 Effect of the gas velocity $\langle u\rangle_{g,o}$ on the conversion efficiency and the junction temperatures. $Z_eT_o=0.59$, $R^*_{e,o}=1$, $\tau_c=10$ s, $D_1=1.3$ mm, $l_s=0.6$ mm, $L_{TE}=60$ mm, $L_C=7.5$ mm, $C_{TE}=1908.8$, $C_C=3236.0$, $k^*_{TE}=75$, $k^*_C=523.6$, $\Phi=0.414$.

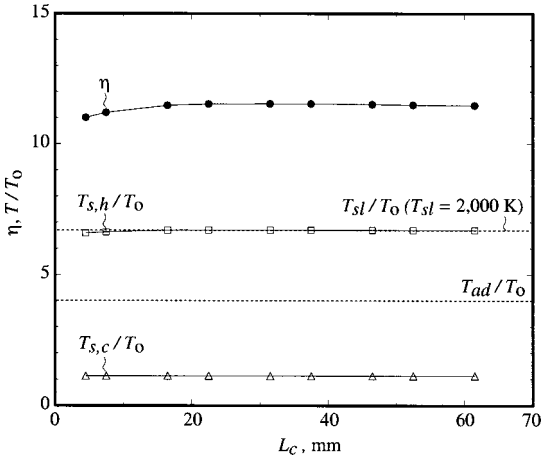

Fig. 6 Effect of the combustion region length L_C on the conversion efficiency and the junction temperatures. $Z_eT_o=0.59$, $R^*_{e,o}=1$, $\tau_c=10$ s, $\langle u\rangle_{g,o}=0.75$ m/s, $D_1=1.3$ mm, $l_s=0.6$ mm, $L_{TE}=60$ mm, $C_{TE}=1908.8$, $C_C=3236.0$, $k^*_{TE}=75$, $k^*_C=523.6$, $\Phi=0.414$.

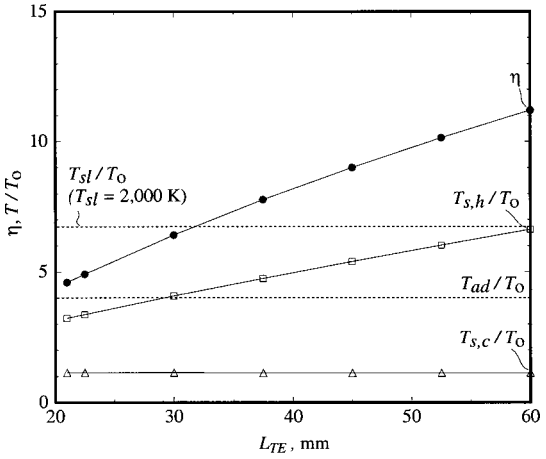

Fig. 8 Effect of the thermoelectric region length L_{TE} on the conversion efficiency and the junction temperatures. $Z_eT_o=0.59$, $R^*_{e,o}=1$, $\tau_c=10$ s, $\langle u\rangle_{g,o}=0.75$ m/s, $D_1=1.3$ mm, $l_s=0.6$ mm, $L_C=7.5$ mm, $C_{TE}=1908.8$, $C_C=3236.0$, $k^*_{TE}=75$, $k^*_C=523.6$, $\Phi=0.414$.

ing temperature. Then within the chemical kinetic considered, there is no limit on the achievable maximum flame temperature.

The efficiency increases with an increase in the length of the thermoelectric region, as shown in Fig. 8. Here, $L_{TE}=60$ mm is used to optimize the efficiency and keep $T_{s,h}\leqslant T_{sl}=2000$ K.

Improved surface convection between the gas and solid phase results in the higher temperature and the higher efficiency. This requires large specific interfacial area [in the surface convection terms $Q_{g,ku}$ and $Q_{s,ku}$ of Eqs. (4) and (9) respectively] and large Nusselt number. The specific interfacial area $A_{sg}/V(=4D_1/(2l_s+D_1)^2)$ have a maximum value at $D_{1,opt}=2l_s$ for a fixed l_s. However, the optimum inside diameter for the maximum efficiency will be different from than $D_{1,opt}$, since the relative magnitude of the other terms in the energy conservation equations of Eqs. (14) and (19), are dependent on D_1 and l_s. As shown in Fig. 9, the maximum efficiency is achieved near $D_1=1.3$ mm, for $l_s=0.6$ mm, which is close to the optimum diameter $D_{1,opt}=1.2$ mm. The optimum diameter is also restricted by the allowable hot junction temperature being below the melting temperature T_{sl}.

As the tube thickness l_s decreases, the conduction heat loss decreases and thus the hot junction temperature increase. While keeping the hot junction temperature $T_{s,h}\leqslant T_{sl}$, $l_s=0.6$ mm gives the highest efficiency, as shown Fig. 10. If a higher melting temperature is allowed, the tube wall thickness smaller than 0.6 mm would give even higher efficiency. However, as the l_s is decreased beyond a threshold, the Joule heating becomes very significant and the efficiency begins to decrease.

Figure 11 shows the effect of the electrical resistance ratio on the conversion efficiency. The efficiency does not increase noticeably for $R^*_{e,o}>1.27$. For simplicity, $R^*_{e,o}=1$ is used to optimize the efficiency. For the unity $R^*_{e,o}$, the total internal resistance $2N_tR_e$ is matched with the external resistance $R_{e,o}$. The power generated, and the current and voltage, are regulated by combining modules in parallel or series arrangements to meet the requirement.

In general, the surface radiation in the tube deteriorates the conversion efficiency by lowering the hot junction temperature. Here, the blackbody emissivity, $\epsilon_r=1$, is used for the surface

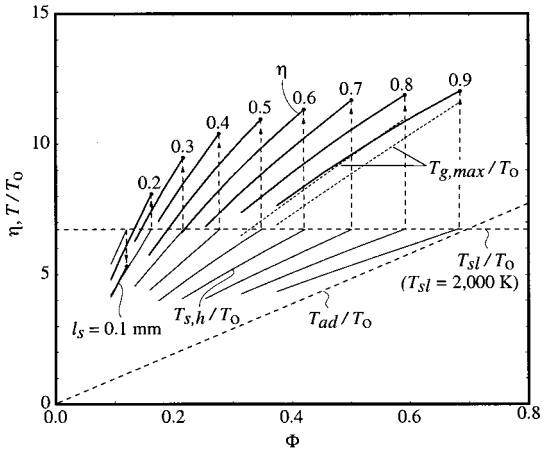

Fig. 7 Effect of the stoichiometric ratio Φ on the conversion efficiency and the hot junction temperature, for various tube wall thicknesses. $Z_eT_o=0.59$, $R^*_{e,o}=1$, $\tau_c=10$ s, $\langle u\rangle_{g,o}=0.75$ m/s, $D_1=1.3$ mm, $L_{TE}=60$ mm, $L_C=7.5$ mm, $C_{TE}=1908.8$, $C_C=3236.0$, $k^*_{TE}=75$, $k^*_C=523.6$.

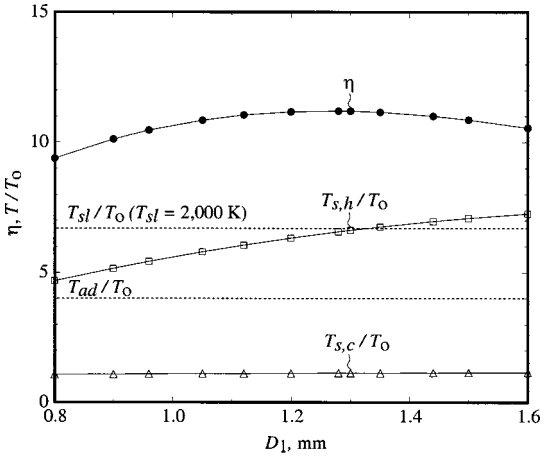

Fig. 9 Effect of the diameter D_1 of the thermoelectric regions on the conversion efficiency and the junction temperatures. $Z_eT_o=0.59$, $R^*_{e,o}=1$, $\tau_c=10$ s, $\langle u\rangle_{g,o}=0.75$ m/s, $l_s=0.6$ mm, $L_{TE}=60$ mm, $L_C=7.5$ mm, $C_{TE}=1908.8$, $C_C=3236.0$, $k^*_{TE}=75$, $k^*_C=523.6$, $\Phi=0.414$.

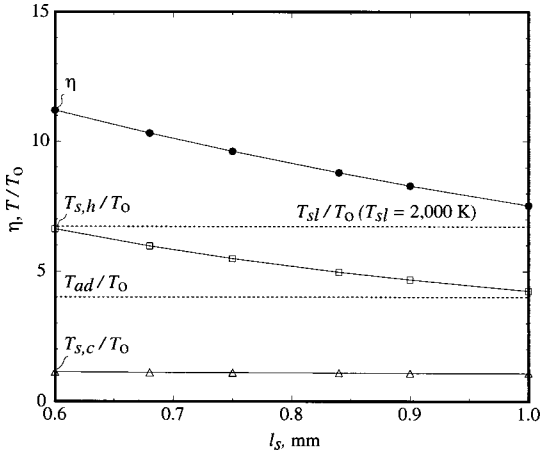

Fig. 10 Effect of the tube thickness l_s on the conversion efficiency and the junction temperatures. $Z_eT_o=0.59$, $R^*_{e,o}=1$, $\tau_c=10$ s, $\langle u\rangle_{g,o}=0.75$ m/s, $D_1=1.3$ mm, $L_{TE}=60$ mm, $L_C=7.5$ mm, $C_{TE}=1908.8$, $C_C=3236.0$, $k^*_{TE}=75$, $k^*_C=523.6$, $\Phi=0.414$.

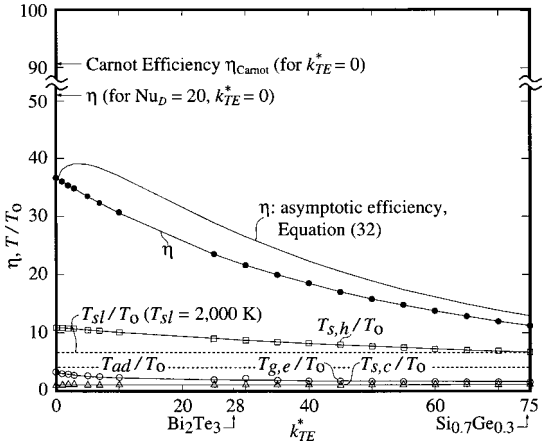

Fig. 12 Effect of the thermal conductivity k_{TE} of the thermoelectric region on the conversion efficiency and the junction temperatures. $R^*_{e,o}=1$, $\tau_c=10$ s, $\langle u\rangle_{g,o}=0.75$ m/s, $D_1=1.3$ mm, $l_s=0.6$ mm, $C_{TE}=1908.8$, $C_C=3236.0$, $L_{TE}=60$ mm, $L_C=7.5$ mm, $k^*_C=523.6$, $\Phi=0.414$.

radiation within the tube. The tube length to diameter ratio is very large, and therefore, the radiation heat transfer is rather local.

Effect of Thermal Conductivity and Melting Temperature. A good thermoelectric material should have a large Seebeck coefficient α_S, and a low thermal conductivity k_{TE} to keep a large temperature difference. It should also have a low electrical resistance ρ_e to minimize the Joule heating. These properties are embodied in a figure-of-merit $Z_e=\alpha_S/(k_{TE}\rho_e)$. The thermal conductivity of the thermoelectric region is a key parameter in limiting the thermoelectric conversion efficiency. Figure 12 shows the effect of thermal conductivity of the thermoelectric region k_{TE} on the efficiency and the junction temperatures. The efficiency increases rapidly as the thermal conductivity decreases.

For lower thermal conductivity, (such as that of the low-temperature thermoelectric materials, e.g., bismuth telluride Bi_2Te_3, $k_{TE}=1.6$ W/m K, $k^*_{TE}=28$), higher efficiencies are possible. Currently the highly melting temperature material is used.

The asymptotic, quasi-steady, overall energy equation, neglecting radiation losses, gives

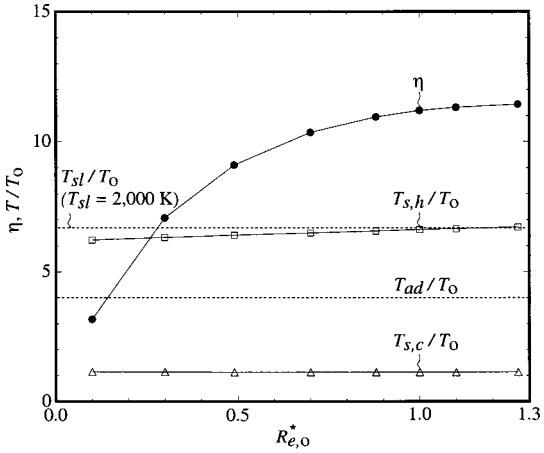

Fig. 11 Effect of the dimensionless external resistance $R^*_{e,o}$ on the conversion efficiency and the junction temperatures. $Z_eT_o=0.59$, $\tau_c=10$ s, $\langle u\rangle_{g,o}=0.75$ m/s, $D_1=1.3$ mm, $l_s=0.6$ mm, $C_{TE}=1908.8$, $C_C=3236.0$, $L_{TE}=60$ mm, $L_C=7.5$ mm, $k^*_{TE}=75$, $k^*_C=523.6$, $\Phi=0.414$.

$$\eta=\frac{J_e^2R_{e,o}/N_t}{Q_e+Q_{g,u}+J_e^2R_{e,o}/N_t}. \tag{28}$$

The neglected radiation losses to the ambient are less than 1 ~3 percent of the combustion heating rate. This is because due to the high aspect ratio, the high temperature region of the tube is barely exposed to the ambient and the cold ends.

Assuming a linear solid temperature distribution, the external heat removal rate at the cold junctions Q_e is approximated by the sum of the conduction loss and the cold-junction Peltier loss. Then from Eq. (26) we have

$$Q_e=\mathrm{Nu}_e\frac{k_g}{D_2}A_s[(T_{s,1}-T_o)+(T_{s,n}-T_o)]$$

$$=2k_{TE}A_s\frac{\Delta T_s}{L_{TE}}+J_e\alpha_S(T_{s,1}+T_{s,n}). \tag{29}$$

The exhaust gas heat loss $Q_{g,u}$ is

$$Q_{g,u}=(\rho c_pA)_g\langle u\rangle_g(T_{g,e}-T_o), \tag{30}$$

where $T_{g,e}$ is the exhaust gas temperature.

The power generated from a tube $J_e^2R_{e,o}/N_t$ is, from Eq. (21)

$$J_e^2R_{e,o}/N_t=\frac{\alpha_S^2\Delta T_s^2R^*_{e,o}}{2\rho_eL_{TE}(1+R^*_{e,o})^2}A_s. \tag{31}$$

Then, the efficiency given by Eq. (28), becomes

$$\eta^{-1}=1+\frac{1}{Z_eT_o}\frac{4(1+R^*_{e,o})}{R^*_{e,o}}\frac{T_o}{\Delta T_s}+\frac{1+R^*_{e,o}}{R^*_{e,o}}\frac{T_{s,c}}{\Delta T_s}+\frac{2}{Z_eT_o}$$
$$\times\frac{(1+R^*_{e,o})^2}{R^*_{e,o}}\frac{(\rho c_p\langle u\rangle T)_{g,e}-(\rho c_p\langle u\rangle T)_{g,o}}{k_{TE}\dfrac{\Delta T_s}{L_{TE}}}\frac{D_1^2}{D_2^2-D_1^2}\frac{T_o}{\Delta T_s}. \tag{32}$$

The prediction of Eq. (32) is also shown in Fig. 12. The difference between Eq. (32) and the numerical results is mainly due to the underestimation of the conduction loss due to the convex, nonlinear solid temperature distribution. The convex solid temperature profile becomes more pronounced for the low thermal conductivity materials. In Eq. (32), the underestimation of the conduction loss leads to an overestimation of the asymptotic efficiency. In Fig. 12, as the thermal conductivity decreases, and therefore, the conduction loss decreases, the asymptotic efficiency

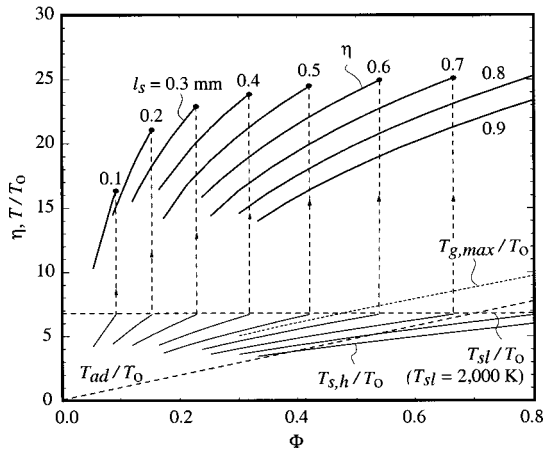

Fig. 13 Effect of the stoichiometric ratio Φ on the conversion efficiency and the hot junction temperature, for various tube wall thicknesses for low thermal conductivity material (Bi_2Te_3). $Z_eT_o=1.58$, $R^*_{e,o}=1$, $\tau_c=10$ s, $\langle u\rangle_{g,o}=0.75$ m/s, $D_1=0.63$ mm, $L_{TE}=60$ mm, $L_C=7.5$ mm, $C_{TE}=1908.8$, $C_C=3236.0$, $k^*_{TE}=28$, $k^*_C=523.6$.

becomes close to that obtained numerically. Figure 12 shows that due to the exhaust gas enthalpy loss, the maximum efficiency for zero thermal conductivity, $k^*_{TE}=0$, is 37 percent, under the baseline conditions listed in Table 1. Note that the maximum efficiency is lower than the Carnot efficiency (due to the exhaust gas enthalpy, the Joule heating, and the cold-junction Peltier heating losses). Also note that for a larger Nusselt number, say $Nu_D=20$ (that is, for enhanced surface convection), resulting in a reduction in the exhaust gas enthalpy loss, the maximum efficiency increases substantially (but is still lower than the Carnot efficiency, due to the Joule and the cold-junction Peltier heating losses).

The solid conduction is always unfavorable for achieving a higher junction temperature difference and a higher conversion efficiency. This is in contrast to the unidirectional flow arrangement in which the solid conduction is the main mechanism for the heat recirculation for achieving a superadiabatic temperature (along with surface radiation).

Figure 13 shows that for a low thermal conductivity material, say $k^*_{TE}=28$, a conversion efficiency over 25 percent is achievable, while $T_{s,h}$ is kept below $T_{sl}=2000$ K. Optimizations have shown that for this k^*_{TE} a smaller tube diameter, $D_1=0.63$ mm, is needed and the results shown in Fig. 13, use this diameter. Note that using $k^*_{TE}=28$, with $D_1=0.63$ mm and $\Phi=0.53$, the electrical power generated is the same as that for $k^*_{TE}=75$, $D_1=1.3$ mm and $\Phi=0.414$. However, much less fuel is used. The smaller gas flow cross-sectional area results in a saving of 61 percent of the fuel. This is due to the smaller solid conduction loss.

The reduction in the effective thermal conductivity, potentially achievable using small powders (small grain size), should lead to a high efficiency thermoelectric converter. Experimental verification of the high efficiency thermoelectric power generator is needed.

Conclusion

The proposed combustion-thermoelectric tube allows for harvesting of the local superadiabatic temperature and the analysis of the combustion-thermoelectric energy conversion efficiency. Direct fuel injection is effective in controlling the flame position and in increasing the flame and the hot junction temperatures. For the current high-temperature $Si_{0.7}Ge_{0.3}$ thermoelectric alloy, a conversion efficiency of 11.3 percent is predicted. For a thermal conductivity equal to that of bismuth telluride Bi_2Te_3, and a melting temperature of 2000 K, a conversion efficiency of about 25 percent is predicted.

Nomenclature

a = frequency factor (s^{-1}) or length (mm)
A_g = cross-sectional area of gas phase $\pi D_1^2/4$ (m^2)
A_s = cross-sectional area of solid phase $\pi(D_2^2-D_1^2)/4$ (m^2)
A_r = surface area for surface radiation $\pi D_1\Delta x$ (m^2)
A_{sg} = interfacial surface area $\pi D_1\Delta x$ (m^2)
c_p = specific heat capacity (J/kg K)
C = heat capacity ratio $\rho c_p/(\rho c_p)_g$
D_1, D_2 = inside and outside diameter (m)
D_m = diffusion coefficient (m^2/s)
E_b = blackbody emissive power (W/m^2)
F_{i-j} = view factor
J_e = current (A)
k = thermal conductivity (W/m K)
l_s = tube wall thickness $(D_2-D_1)/2$ (m)
L = length (m)
Le = Lewis number $D_m/\alpha_g=(\rho c_p)_g D_m/k_g$
M = molar weight (kg/kmole)
n = n-type material or number of grid nodes
$\dot{n}_{r,P}$ = volumetric production rate of species P (kg/m^3 s)
N_t = number of thermoelectric tube
Nu_D = internal Nusselt number
Nu_e = external Nusselt number
p = p-type material or pressure (Pa)
P = combustion product species
q = heat flux (W/m^2)
Q = heat flow rate (W)
Q_k = conduction heat flow rate (W)
Q_{ku} = surface-convection heat flow rate (W)
Q_u = convection heat flow rate (W)
Q_r = surface radiation heat flow rate (W)
R_e = internal electrical resistance per a tube (Ohm)
$R_{e,o}$ = external electrical resistance (Ohm)
R = universal gas constant 8.3145 kJ/kmole K
Re_D = Reynolds number $\rho_g\langle u\rangle_{g,o}D_1/\mu_g$
$\dot{S}$ = energy conversion rate (W)
t = time (s)
T = temperature (K)
$\langle u\rangle_g$ = average gas velocity (m/s)
V = nodal volume of gas and solid phases (m^3)
x = coordinate axes (m)
x_{cs} = coordinate of control surface of a grid (m)
Z_e = figure of merit of the thermoelectric material $\alpha_S^2/(\rho_e k_{TE})$(1/K)

Greek

α_S = Seebeck coefficient (V/K)
δx = distance between nodes (m)
ΔE_a = activation energy (kJ/kmole)
$\Delta h_{r,F}$ = heat of reaction of fuel (J/kg fuel)
ΔT_s = $T_{s,h}-T_{s,c}$ (K)
Δx = length of nodal control volume (m)
$\Delta\varphi$ = voltage (V)
ϵ_r = emissivity
Φ = stoichiometric ratio
η = conversion efficiency $(J_e^2R_{e,o}/N_t)/(-\Delta h_{r,F}\rho_{F,o}\langle u\rangle_g A_g)$
ν = stoichiometric coefficient
ρ = density (kg/m^3)
ρ_e = internal electric resistivity (Ohm m)
σ_{SB} = Stefan–Boltzmann constant 5.670×10^{-8} W/m^2-K^4
τ_c = period of reciprocation (s)

Subscripts

1,2,...,$n+2$ = node index
a = activation
ad = adiabatic
b = blackbody
c = cold or combustion or cycle
cs = control surface
C = combustion
D = diameter
e = electric or external or east or exhaust
F = fuel
g = gas phase
h = hot
i,j = node index
J = Joule
k = conduction
ku = surface convection
l = left
m = mass diffusion
n = n-type material or last node
o = reference or outgoing
opt = optimum value
O = oxidant
p = pressure or p-type material
P = Peltier or product species
r = radiation or reaction or right
R = reactant species
s = solid phase
sg = solid-gas interface
sl = solid-liquid phase change
st = stoichiometry
S = Seebeck
SB = Stefan–Boltzmann
t = tube
TE = thermoelectric
u = convection
w = west
x = x-component

Other symbols

$\langle\ \rangle$ = local spatial averaged
* = dimensionless quantity

References

[1] Hanamura, K., Echigo, R., and Zhdanok, S. A., 1993, ''Superadiabatic Combustion in a Porous Medium,'' Int. J. Heat Mass Transf., **36**, No. 13, pp. 3201–3209.
[2] Min, D. K., and Shin, H. D., 1991, ''Laminar premixed flame stabilized inside a honeycomb ceramic,'' Int. J. Heat Mass Transf., **34**, No. 2, pp. 341–356.
[3] Sahraoui, M., and Kaviany, M., 1994, ''Direct simulation vs volume-averaged treatment of adiabatic, premixed flame in a porous medium,'' Int. J. Heat Mass Transf., **37**, No. 18, pp. 2817–2834.
[4] Hoffmann, J. G., Echigo, R., Tada, S., and Yoshida, H., 1996, ''Analytical Study of Flame Stabilization in Reciprocating Combustion in Porous Media with High Thermal Conductivity,'' *26th Symposium (International) on Combustion*, pp. 2709–2716.
[5] Hoffmann, J. G., Echigo, R., Yoshida, H., and Tada, S., 1997, ''Experimental Study on Combustion in Porous Media with a Reciprocating Flow System,'' Combust. Flame, **111**, pp. 32–46.
[6] Echigo, R., Hanamura, K., Yoshida, H., Koda, M., and Tawata, K., 1992, ''Sophisticated Thermoelectric Conversion Devices of Porous Materials by Super-Adiabatic Combustion of Reciprocating Flow and Advanced Power Generation System,'' *11th International Conference on Thermoelectrics*, pp. 45–50.
[7] Rowe, D. M., Editor, 1995, *CRC Handbook of Thermoelectrics*, CRC Press, Boca Raton.
[8] Chen, G., 1998, ''Thermal conductivity and ballistic-phonon transport in the cross-plane direction of superlattices,'' Phys. Rev. B, **57**, No. 23, pp. 14958–14973.
[9] Kesting, A., Pickenacker, O., Trimis, D., and Drust, F., 1999, ''Development of a Radiation Burner for Methane and Pure Oxygen Using the Porous Burner Technology,'' *5th International Conference on Technologies and Combustion for a Clean Environment (Clean Air V)*, Lisbon, Portugal.
[10] Yoshizawa, Y., Sasaki, K., and Echigo, R., 1988, ''Analytical study of the structure of radiation controlled flame,'' Int. J. Heat Mass Transf., **31**, No. 2, pp. 311–319.
[11] Kaviany, M., 1999, *Principles of Heat Transfer in Porous Media*, Corrected Second Edition, Springer-Verlag, New York.
[12] Siegel, R., and Howell, J. R., 1992, *Thermal Radiation Heat Transfer*, Third Edition, Hemisphere, Washington, D.C.
[13] Kaviany, M., 2000, *Principles of Heat Transfer*, Course Pack, University of Michigan.
[14] Patankar, S. V., 1980, *Numerical Heat Transfer and Fluid Flow*, Hemisphere, Washington, DC.